CHEMISTRY OF MATERIALS

pubs.acs.org/cm

Article

Tuning between Proper and Hybrid-Improper Mechanisms for Polar Behavior in $CsLn_2Ti_2NbO_{10}$ Dion-Jacobson Phases

Vanessa A. Cascos, Jennifer Roberts-Watts, Chloe Skingle, Igor Levin, Weiguo Zhang, P. Shiv Halasyamani, Martin C. Stennett, Neil C. Hyatt, Eric Bousquet,* and Emma E. McCabe*

Cite This: *Chem. Mater.* 2020, 32, 8700–8712

Read Online

ACCESS | Metrics & More | Article Recommendations | Supporting Information

ABSTRACT: The Dion-Jacobson (DJ) family of perovskite-related materials have recently attracted interest due to their polar structures and properties, resulting from hybrid-improper mechanisms for ferroelectricity in $n = 2$ systems and from proper mechanisms in $n = 3$ $CsBi_2Ti_2NbO_{10}$. We report here a combined experimental and computational study on analogous $n = 3$ $CsLn_2Ti_2NbO_{10}$ (Ln = La, Nd) materials. Density functional theory calculations reveal the shallow energy landscape in these systems and give an understanding of the competing structural models suggested by neutron and electron diffraction studies. The structural disorder resulting from the shallow energy landscape breaks inversion symmetry at a local level, consistent with the observed second-harmonic generation. This study reveals the potential to tune between proper and hybrid-improper mechanisms by composition in the DJ family. The disorder and shallow energy landscape have implications for designing functional materials with properties reliant on competing low-energy phases such as relaxors and antiferroelectrics.

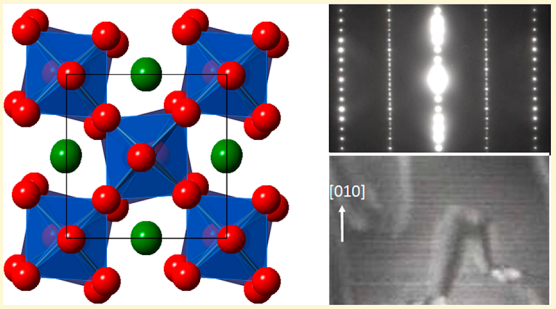

1. INTRODUCTION

Ferroelectrics are widely used in applications such as sonars and sensors,[1] electrooptics,[2] capacitors,[3] and memory devices,[4] making them materials of significant technological importance. From an academic perspective, the origins of their switchable polarization are fascinating as they hold the key to designing new classes of polar materials.[5−7] In proper ferroelectrics, polar displacive distortions (e.g., of cations relative to anions in the structure) form the primary order parameter and drive the paraelectric−ferroelectric phase transition to give the polar, noncentrosymmetric phase.[8] Such displacements are often favored by particular electronic configurations of ions (e.g., "inert pair" Bi^{3+}, Pb^{2+} ions, and d^0 transition metal ions). Alternatively, hybrid-improper mechanisms for ferroelectricity rely on coupling nonpolar distortions (such as rotations of octahedra in layered perovskite-related materials) to break inversion symmetry and stabilize polar displacements.[9,10] This opens up the possibility of preparing new families of polar materials. These two mechanisms give distinctly different temperature-dependence of polar characteristics such as permittivity and therefore the possibility to tune the temperature scale and range of functional properties.

Families of layered perovskite-related materials are ideal systems in which to explore the mechanisms that give rise to polar structures.[5] Recent work on hybrid-improper Ruddlesden−Popper phases[11,12] has shown that nonpolar distortions such as octahedral rotations often give relatively small energy gains (compared with polar cation displacements in proper systems) and that different rotation modes can have similar energy gains. This gives a fairly shallow energy landscape with competing ground states and hence the potential to switch between phases giving more complex behavior such as antiferroelectricity,[12] negative thermal expansion,[13,14] and relaxor behavior.[15] This provides a powerful motivation to understand the competition between different mechanisms/distortions and the consequences for structure and properties.

The Dion-Jacobson (DJ) family of perovskite-related materials have been a key focus for exploring hybrid-improper mechanisms for ferroelectricity.[16] These layered materials, of general formula $A'A_{n-1}B_nO_{3n+1}$, are built up from perovskite-like layers (of corner-linked BO_6 octahedra) n layers thick, separated by layers of large A' ions (e.g., Cs^+, Rb^+). The A sites within the perovskite-like blocks are typically occupied by lanthanide or group 2 ions. In contrast to the Ruddlesden−Popper and Aurivillius families, the perovskite-like blocks in DJ materials are eclipsed, giving ideal, high-symmetry structures of $P4/mmm$ symmetry (Figure 1).

Received: August 14, 2020
Revised: September 22, 2020
Published: September 22, 2020

https://dx.doi.org/10.1021/acs.chemmater.0c03326
Chem. Mater. 2020, 32, 8700−8712

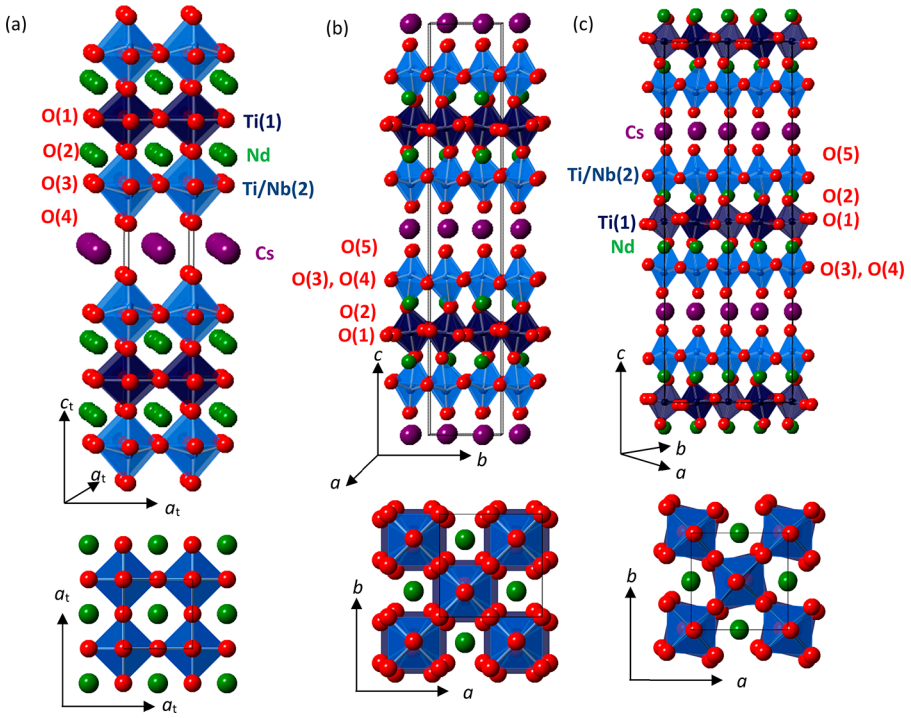

Figure 1. Illustration of crystal structures for n = 3 DJ phases including (a) ideal *P*4/*mmm* high symmetry model, (b) *Imcm* model for $CsNd_2Ti_2NbO_{10}$ at 700 K (with disordered O(1) site) with A_5^+ rotations about in-plane axis, and (c) *Pbnm* structure for $CsNd_2Ti_2NbO_{10}$ at 293 K with A_5^+ and M_3^+ rotations. Cs, *Ln*, and O sites are shown by purple, green, and red spheres, and Ti(1) and Ti/Nb(2) sites are within dark blue and light blue polyhedra, respectively.

Theoretical work has shown that for even-layer DJ phases, combinations of rotations of BO_6 octahedra (e.g., about both an in-plane axis and about the tetragonal axis $[001]_t$ to give $a^-a^-c^+$ tilts overall) can break inversion symmetry, stabilizing polar, noncentrosymmetric structures by hybrid-improper mechanisms.[16] Zhu et al. have explored the role of A' ions (Cs^+, Rb^+) in stabilizing different combinations of rotation modes and how these ions influence the sequence of phase transitions to the centrosymmetric, nonpolar high temperature phase.[17,18]

While combinations of equivalent rotation modes (i.e., involving rotation of all octahedra about both in-plane and out-of-plane axes) in odd-layered DJ systems do not break inversion symmetry,[16] distortions involving rotation of only inner-layer octahedra, or only outer-layer octahedra about $[001]_t$ are possible,[19−21] and can couple with rotations about an in-plane axis to break inversion symmetry.[20] This means that odd-layer DJ phases can adopt polar structures stabilized by proper or hybrid-improper mechanisms. Recent work on $CsBi_2Ti_2NbO_{10}$ showed that with $6s^2$ Bi^{3+} ions on the *A* sites (which favor asymmetric coordination environments[22]), the origin of its polar behavior is close to a proper mechanism.[20] Experimental studies of $RbBi_2Ti_2NbO_{10}$ and $CsBi_2Ti_2TaO_{10}$ suggest these closely related materials behave analogously.[23] However, the possibility of tuning between proper and hybrid-improper mechanisms and the role of *A* cations in these systems has not been explored.

We report here a combined experimental and computational study of the n = 3 DJ phases $CsLn_2Ti_2NbO_{10}$ (*Ln* = La, Nd). Our structural characterization using neutron and electron diffraction gives an understanding of the crystal structure at long-range and shorter length scales. Density functional theory calculations reveal the very shallow energy landscape in these systems, and competing combinations of octahedral rotations can induce disorder and break inversion symmetry at a local level, as manifested in the second-harmonic generation behavior. These results indicate that DJ phases can be tuned between proper and hybrid-improper mechanisms but that the hybrid-improper behavior may be limited to effects at short length scales.

2. METHODS

Polycrystalline samples of $CsLa_2Ti_2NbO_{10}$ and $CsNd_2Ti_2NbO_{10}$ were prepared by reacting stoichiometric quantities of Cs_2CO_3 (in 30% excess to account for volatility), La_2O_3, Nd_2O_3, TiO_2, and Nb_2O_5 [these reagents were of ≥99.5% purity and were dried (at 800−1000 °C) prior to use]. These reagents were ground by hand in an agate mortar and pestle under an acetone slurry and pressed into 10 mm diameter pellet(s). The resulting mixture was placed in an alumina boat and heated at 550 °C for 6 h followed by 12 h at 1000 °C. After cooling to room temperature in the furnace, the sample was ground under acetone and reheated at 1000 °C for 12 h, with this process repeated several times. Finally, the powder was washed several times with cold, deionized water and recovered by vacuum filtration. Preliminary characterization was carried out using X-ray powder diffraction (XRPD) using a Bruker D8 Advance diffractometer operating in reflection mode with a Cu Kα source and a Vantec detector. (Certain commercial equipment, instruments, or materials are identified in this paper in order to specify the experimental procedure adequately. Such identification is not intended to imply recommendation or endorsement by NIST, nor is it intended to imply that the materials or equipment identified are necessarily the best available for the purpose.)

Neutron powder diffraction data were collected on the BT1 diffractometer at the NIST Center for Neutron Research (NCNR). Data sets were collected at 20, 293, 400, and 700 K. Diffraction data were analyzed using the Rietveld method[24] in the Topas Academic software.[25,26] Distortions and group-subgroup relations were explored using the symmetry-adapted distortion mode approach and

https://dx.doi.org/10.1021/acs.chemmater.0c03326
Chem. Mater. 2020, 32, 8700−8712

Table 1. Summary of Symmetry analysis for n = 3 DJ Phases (With Parent High Symmetry Structure of $P4/mmm$ Symmetry) based on Analysis by Aleksandrov[47] and Using ISODISTORT,[27] Expressed with ψ and φ Representing In-phase and Out-of-phase Rotations, Respectively, and Using Glazer Notation[40]

irrep	Aleksandrov notation	glazer notation	symmetry	unit cell
A_5^+	$\varphi 00$ $-\varphi 00$	$a^-b^0c^0$ $-(a^-b^0c^0)$	$Fmmm$	$2a_t \times 2a_t \times 2c_t$
	$\varphi\varphi 0$ $-\varphi$ $-\varphi 0$	$a^-a^-c^0$ $-(a^-a^-c^0)$	$Imcm$	$\sqrt{2}a_t \times \sqrt{2}a_t \times 2c_t$
M_5^+	$\varphi 00$ $\varphi 00$	$a^-b^0c^0$ $a^-b^0c^0$	$Cmma$	$2a_t \times 2a_t \times c_t$
	$\varphi\varphi 0$ $\varphi\varphi 0$	$a^-a^-c^0$ $a^-a^-c^0$	$Pmna$	$\sqrt{2}a_t \times c_t \times \sqrt{2}a_t$
A_3^+	00φ $00-\varphi$	$a^0a^0c^-$ $-(a^0a^0c^-)$	$I4/mcm$	$\sqrt{2}a_t \times \sqrt{2}a_t \times 2c_t$
M_3^+	00φ 00φ or 00ψ 00ψ	$a^0a^0c^-$ $a^0a^0c^-$	$P4/mbm$	$\sqrt{2}a_t \times \sqrt{2}a_t \times c_t$
A_1^-	00φ 00φ (outer only)	$a^0a^0c^-$ $a^0a^0c^-$ (outer only)	$I4/mcm$	$\sqrt{2}a_t \times \sqrt{2}a_t \times 2c_t$
M_1^-	00ψ 00ψ (outer only)	$a^0a^0c^+$ $a^0a^0c^+$ (outer only)	$P4/nbm$	$\sqrt{2}a_t \times \sqrt{2}a_t \times c_t$
$A_5^+ + A_3^+$	$\varphi\varphi\varphi$ $-\varphi-\varphi-\varphi$	$a^-a^-c^-$ $-(a^-a^-c^-)$	$C2/c$	$2c_t \times \sqrt{2}a_t \times \sqrt{2}a_t$
$A_5^+ + M_3^+$	$\varphi\varphi\varphi$ $-\varphi-\varphi\varphi$ or $\varphi\varphi\psi$ $-\varphi-\varphi$ ψ	$a^-a^-c^-$ $-(a^-a^-)c^-$	$Pbnm$	$\sqrt{2}a_t \times \sqrt{2}a_t \times 2c_t$
$A_5^+ + A_1^-$ $(+\Gamma_5^-)$	$\varphi\varphi\varphi$ $-\varphi-\varphi\varphi$ (outer only)	$a^-a^-c^-$ $-(a^-a^-)c^-$ (outer only)	$I2\ cm$	$\sqrt{2}a_t \times \sqrt{2}a_t \times 2c_t$
$A_5^+ + M_1^-$	$\varphi\varphi\psi$ $-\varphi-\varphi\psi$ (outer only)	$a^-a^-c^+$ $-(a^-a^-)c^+$ (outer only)	$Pnna$	$\sqrt{2}a_t \times 2c_t \times \sqrt{2}a_t$
$M_5^+ + A_3^+$	$\varphi\varphi\varphi$ $\varphi\varphi-\varphi$	$a^-a^-c^-$ $a^-a^-c^-$	$Pbcn$	$\sqrt{2}a_t \times \sqrt{2}a_t \times 2c_t$
$M_5^+ + M_3^+$	$\varphi\varphi\varphi$ $\varphi\varphi\varphi$	$a^-a^-c^-$ $a^-a^-c^-$	$C2/m$	$2a_t \times 2a_t \times c_t$
$M_5^+ + A_1^-$	$\varphi\varphi\varphi$ $\varphi\varphi\varphi$ (outer only)	$a^-a^-c^-$ $a^-a^-c^-$ (outer only)	$Pbcn$	$\sqrt{2}a_t \times \sqrt{2}a_t \times 2c_t$
$M_5^+ + M_1^-$ $(+\Gamma_5^-)$	$\Phi 0\psi$ $\varphi 0\psi$ (outer only)	$a^-b^0c^+$ $a^-b^0c^+$ (outer only)	$Abm2$	$c_t \times 2a_t \times 2a_t$
	$\varphi\varphi\psi$ $\varphi\varphi\psi$ (outer only)	$a^-a^-c^+$ $a^-a^-c^+$ (outer only)	$Pnc2$	$c_t \times \sqrt{2}a_t \times \sqrt{2}a_t$

ISODISTORT.[27] With the use of a global atomic displacement parameter for all sites, the distribution of Ti and Nb over the two B sites was refined (with a constraint to maintain stoichiometry). This suggested that the central $B(1)$ site is fully occupied by Ti with the outer $B(2)$ occupied equally by Ti and Nb. Ti and Nb have neutron scattering lengths of opposite signs [7.054(3) fm for Nb, −3.438(2) fm for Ti][28] which lead to low average scattering for the mixed sites; therefore, the atomic displacement parameters were constrained to be the average of those of the other sites in the structure. In subsequent refinements, the Ti/Nb distribution was fixed and again, average temperature factors were used for these sites.[20] Separately from the Rietveld analysis described above, the diffuse scatter was fitted by a Warren-like function using the Profit software to estimate the size of sort-ranged correlated regions.

Samples for transmission electron microscopy were prepared by the mechanical grinding and polishing of sintered (1300 °C for 12 h) pellets followed by ion polishing at 100 K until perforation. Selected samples were prepared by grinding the crushed powder under acetone using an agate mortar and pestle and dispersing this suspension on copper grids coated with lacey carbon. Electron diffraction patterns and diffraction-contrast images were obtained in a conventional TEM operated at 200 kV.

$CsLa_2Ti_2NbO_{10}$ and $CsNd_2Ti_2NbO_{10}$ were tested for a second harmonic generation (SHG) signal using the experimental setup described in reference;[29] pellets of $CsLn_2Ti_2NbO_{10}$ were ground and sieved into distinct particle size ranges (<20, 20−45, 45−63, 63−75, 75−90, and 90−125 μm). Relevant comparisons with known SHG materials were made by grinding and sieving crystalline KH_2PO_4 (KDP) into the same particle size ranges. SHG intensity was recorded for each particle size range.

Diffuse reflectance spectra were recorded by placing sample ground with dry sodium chloride (~10% w/w) in an optical cuvette and illuminating it with a halogen lamp (Ocean Optics DH-2000-S). Nonspecular scattered light was collected, and the spectrum was recorded using an OceanOptics spectrometer (Mayer2000 Pro). A cuvette of ground sodium chloride was used as a reference. The data were used to calculate the reflectance spectra R(I) and Kubelka−Munk spectra F(R).[30]

Pellets of $CsLa_2Ti_2NbO_{10}$, 5 mm in diameter, were heated at 2 °C min^{-1} to 1000 °C and held at this temperature for 4 h. During this sintering process, the pellets were embedded in a sacrificial powder of the same composition. This gave pellets of density ~71% of their theoretical density. Gold electrodes were attached to sintered pellets of $CsLn_2Ti_2NbO_{10}$ (Ln = La, Nd) using gold paste (annealed at 800 °C for 2 h). The dielectric response of these pellets was measured at 10, 100, and 250 kHz using an HP inductance−capacitance−resistance (LCR) meter. Measurements were carried out in a tube furnace, heating the sample at 1 °C min^{-1} to 800 °C.

We performed Density Functional Theory (DFT) calculations using the ABINIT package[31,32] and norm-conserving pseudopotentials from the pseudodojo project (v.3)[33] and generated with the ONCVPSP code.[34] The following orbitals were treated as valence electrons in the pseudopotentials: 2s and 2p for O; 3s, 3p, 3d and 4s for Ti; 4s, 4p, 4d and 5s for Nb; 5s, 5p and 6s for Cs and 5d; and 6s and 6p for La and Nd (the f-electrons are treated as core electrons for Nd such that they do not participate as valence electrons). As in our previous work,[20] we used the virtual crystal approximation (VCA)[35] for the outer $B(2)$ site ($2g$ in the $P4/mmm$ model, see Figure 3a) with an "alchemical" virtual atom made of 50% of Nb and 50% of Ti for this site. We kept a regular Ti atom for the central $B(1)$ site ($1a$ in the $P4/mmm$ model, see Figure 3a). We used the GGA-PBE functional and converged the calculations up to 1 meV/f.u. on energy differences between structural phases and up to 2 cm^{-1} on phonon frequencies by setting the cutoff energy at 50 Hartree for the plane wave expansion and the k-point grid at 6 × 6 × 2 for the integration in the Brillouin zone of the $P4/mmm$ phase and at 3 × 3 × 2 for phases having a doubling of the unit cell with respect to the $P4/mmm$. The phonon frequencies, Born effective charges, dielectric constants, and piezoelectric coefficients were computed through the density functional perturbation theory (DFPT)[36−38] and the polarization through the Berry phase method.[39]

3. RESULTS

3.1. Consideration of Possible Distortions for n = 3 DJ Phases. Perovskite-related materials are well-known to undergo distortions including those involving rotations of BX_6 (X=anion) octahedra and polar or antipolar displacements of ions. The lower-symmetry structures resulting from these distortions have been thoroughly investigated for three-dimensional perovskites.[40−42] The layered nature of the Ruddlesden−Popper and Aurivillius families of materials (with high symmetry structures of $I4/mmm$ symmetry) gives distorted structures of different symmetries depending on whether the perovskite-blocks contain an odd or an even number of layers n of corner-linked BX_6 octahedra.[43−46] Likewise, these distortions have also been explored for DJ phases (with high symmetry structures of $P4/mmm$ symmetry).[47] An added complexity for n = 3 materials of these

https://dx.doi.org/10.1021/acs.chemmater.0c03326
Chem. Mater. 2020, 32, 8700−8712

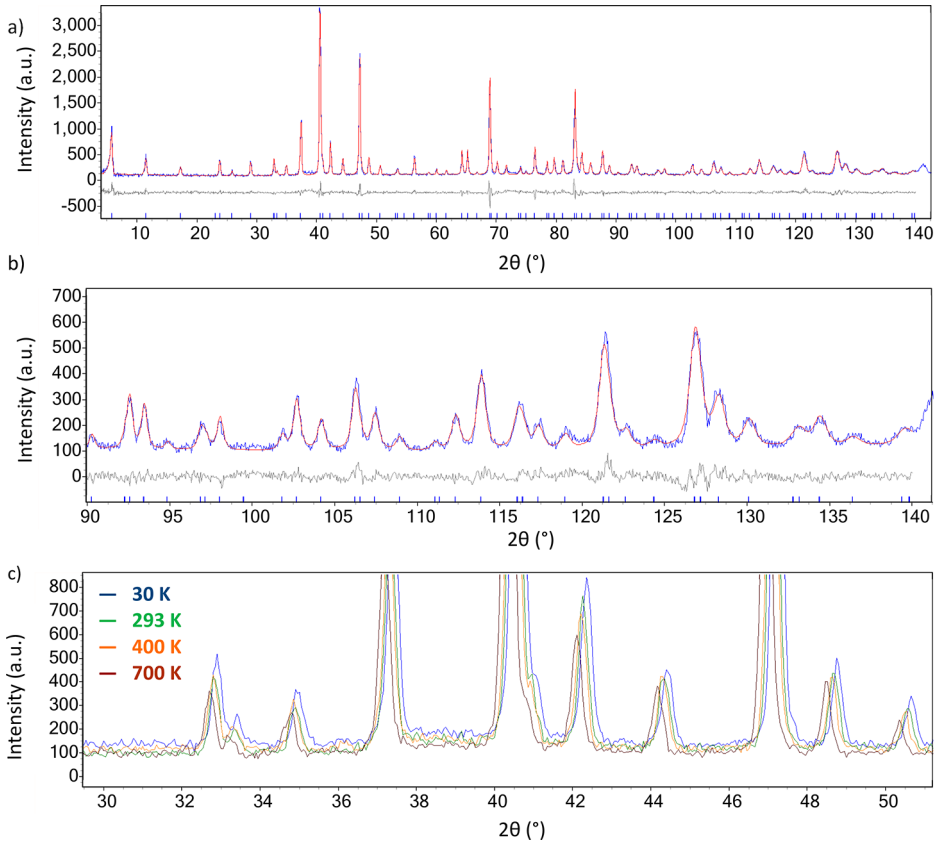

Figure 2. Rietveld refinement profiles for $CsLa_2Ti_2NbO_{10}$ 293 K NPD data fitted with arisotype *P*4/*mmm* model. Observed, calculated, and difference profiles are shown in blue, red, and gray with tick marks for the main phase shown in blue. Upper panel (a) shows whole 2θ range while lower panel (b) shows an enlarged high 2θ region; (c) shows the region of diffuse scatter as a function of temperature with data collected at 30, 293, 400, and 700 K shown by blue open points, green line, orange line, and brown points, respectively.

families (in contrast to n = 1 and n = 2 phases) is the possibility of decoupling rotations of inner and outer BX_6 octahedra about $[001]_t$ (the long, pseudotetragonal axis), i.e., only inner $B(1)X_6$ octahedra (as in $Bi_4Ti_3O_{12}$[19]) or only outer $B(2)X_6$ octahedra (as in $CsBi_2Ti_2NbO_{10}$[20]) might rotate about $[001]_t$. Table 1 summarizes the distortions involving octahedral rotations considered for n = 3 DJ phases using Aleksandrov's notation and Glazer notation, as well as irreps as described by ISODISTORT, and these are illustrated in the Supporting Information.

3.2. Neutron Powder Diffraction. *3.2.1. $CsLa_2Ti_2NbO_{10}$.* Neutron powder diffraction data collected for $CsLa_2Ti_2NbO_{10}$ at 30, 293, 400, and 700 K could be indexed by the aristotype *P*4/*mmm* unit cell. Although no additional reflections are observed, diffuse scattering was observed (e.g., ~37−40° 2θ and 72−74° 2θ) (Figure 2c and Supporting Information). Attempts to fit these NPD data with a model of *P*4/*mmm* symmetry gave an unreasonably high atomic displacement parameter (ADP) for the central equatorial oxygen site O(1). Allowing anisotropy of this ADP suggested significant disorder (either static or dynamic) within the *xy* plane, consistent with rotations of BO_6 octahedra about their axes parallel to the $[001]_t$ direction (see the Supporting Information). Moving this O(1) site from the ideal 2*f* (0 1/2 0) Wyckoff position to a half-occupied 4*n* site (*x* 1/2 0) improved the fit significantly (R_{wp} decreased from 13% (26 parameters) to 9.9% (27 parameters) and gave reasonable ADP values for all sites. Although other lower-symmetry models were considered, including noncentrosymmetric models (see the Supporting Information), our NPD data suggest that the average, long-range structure of $CsLa_2Ti_2NbO_{10}$ as probed by NPD between 30 and 700 K is best described by this disordered model of *P*4/*mmm* symmetry. Refinement profiles and refined parameters for 293 K Rietveld refinement are summarized in Figure 2 and Table 2; those for other temperatures are given in the Supporting Information, along with variable-temperature results. Bond valence sum calculations[48] indicate that while the bonding environments around Cs, Ti(1), and Nb(2) are close to optimal (apparent valences of 1.1, 4.1, and 5.0, respectively), La is slightly overbonded (3.4) while Ti(2) is slightly underbonded (3.8). This illustrates the preference of the slightly larger Nb^{5+} cation (6-coordinate ionic radius 0.64 Å) for the larger outer $B(2)$ site, in which the smaller Ti^{4+} cation (6-coordinate ionic radius 0.605 Å) is slightly underbonded.[49]

The diffuse scattering observed in NPD data changes little with temperature and can be fitted with a Warren-like peak (see Supporting Information), indicative of short-range, two-dimensional correlations.[50] The Warren peak maximum coincided with the approximate position of superstructure reflections due to M-type distortions such as octahedral rotations [k vector = (1/2 1/2 0)] [38.2(1)° 2θ at 700 K; 38.1(1)° 2θ at 30 K, Supporting Information] and suggested correlation lengths within the *ab* plane of ~6 × the in-plane lattice parameter [22(1) Å at 700 K; 24(1) Å at 30 K].

3.2.2. $CsNd_2Ti_2NbO_{10}$. 3.2.2.1. 700 K. In contrast to $CsLa_2Ti_2NbO_{10}$, NPD data collected at 700 K for $CsNd_2Ti_2NbO_{10}$ could not be indexed by the aristotype

https://dx.doi.org/10.1021/acs.chemmater.0c03326
Chem. Mater. 2020, 32, 8700−8712

Table 2. Structural Parameters and Selected Bond Lengths for Refinement for $CsLa_2Ti_2NbO_{10}$ Using 293 K NPD Data[a]

structural parameters			selected bond lengths (Å)	
atom	site	$U_{iso} \times 100$ (Å^2)	Cs − O(4)	8 × 3.161(2)
Cs	1*d*	1.3(1)	La−O(3)	4 × 2.552(2)
La	2*h*; *z* = 0.1410(2)	0.46(6)	La−O(1)	4 × 2.642(2)
Ti(1)	1*a*	0.85(3)	La−O(2)	4 × 2.7358(4)
Ti/Nb(2)	2*g*; *z* = 0.2806(9)	0.85(3)	Ti(1)−O(2)	2 × 1.914(3)
O(1)	4*n*; *x* = 0.118(1)	0.6(1)	Ti(1)−O(1)	4 × 1.979(1)
O(2)	2*g*; *z* = 0.1242(2)	1.10(9)	Ti/Nb(2)−O(4)	1 × 1.78(1)
O(3)	4*i*; *z* = 0.2497(1)	0.61(4)	Ti/Nb(2)−O(3)	4 × 1.984(3)
O(4)	2*g*; *z* = 0.3959(2)	1.06(9)	Ti/Nb(2)−O(2)	1 × 2.41(1)

[a]Refinement carried out in the space group *P*4/*mmm*, *a* = 3.85179(8) Å, *c* = 15.4054(6) Å; R_{wp} = 9.921%, R_p = 7.969%, χ^2 = 1.88; for *P*4/*mmm*, 1*a* is at (0 0 0), 1*d* is at (1/2 1/2 1/2), 2*g* is at (0 0 *z*), 2*h* is at (1/2 1/2 *z*), 4*i* is at (0 1/2 *z*), and 4*n* is at (*x* 1/2 0).

*P*4/*mmm* unit cell and, instead, a larger body-centered $\sqrt{2}a_t \times \sqrt{2}a_t \times 2c_t$ unit cell was required. Pawley refinements using this tetragonal cell were promising, and models of *I*4/*mcm* symmetry (allowing either A_3^+, A_2^+, or A_1^- rotations of BO_6 octahedra around $[001]_t$, see the Supporting Information) were considered. However, the *c* glide perpendicular to [100] (along with the body-centring, giving reflection condition 0*kl* *k*, *l* = 2n) precludes, for example, 0 1 11, 0 1 13, 0 3 3, and 0 3 5 reflections, and therefore, these models were inconsistent with our 700 K data (see the Supporting Information). Although no clear orthorhombic splitting was observed, an orthorhombic model of *Imcm* (*bca* setting of *Imma*, 74) symmetry ($\sqrt{2}a_t \times \sqrt{2}a_t \times 2c_t$) allowing A_5^+ rotations of BO_6 octahedra around $[110]_t$ (see the Supporting Information) gave an excellent fit to the data but an unfeasibly high ADP for the equatorial O(1) site. Allowing this to refine anisotropically suggested disorder in the *ab* plane (consistent with rotation of $Ti(1)O_6$ octahedra about $[001]_t$). Moving O(1) from the high symmetry 8*f* site to the general 16*i* site, consistent with static or dynamic displacement of O(1) in the *ab* plane, gave a chemically reasonable model. Refinement profiles and details are given in the Supporting Information, with selected bond lengths and angles. We note that this model has a metrically tetragonal unit cell, but an orthorhombic symmetry, and it is likely that at length scales shorter than those probed by NPD, the structure may differ from the *Imcm* model as discussed below.

3.2.2.2. 20−600 K. Additional superstructure reflections were observed in 600 K NPD data that were inconsistent with the body-centered *Imcm* symmetry, suggesting a change in structure on cooling (see Figure 3). Various models, allowing combinations of octahedral tilts (see the Supporting Information), were considered and the model of *Pbnm* symmetry (*cab* setting of *Pnma*, 62) gave a good fit to the data. This model allows rotations about the $[110]_t$ and $[001]_t$ axes (A_5^+ and M_3^+ modes, giving $a^-a^-c^-$ tilts; see the Supporting Information).

NPD data collected at 20, 293, and 400 K were also consistent with similar *Pbnm* models, and refinement profiles and refinement details for 293 K data are given in Figure 4 (and in the Supporting Information for other temperatures); selected bond lengths and angles are tabulated in the Supporting Information. The orthorhombic unit cells of *Imcm* and *Pbnm* symmetry proposed to describe the average, long-range structure of $CsNd_2Ti_2Nb_{10}$ are metrically close to being tetragonal, but the orthorhombic symmetry is confirmed (at room temperature) by electron diffraction studies (see below).

Bond valence sum calculations for the 293 K structure give values of 4.3, 3.9, and 5.1 for Ti(1), Ti(2), and Nb(2) sites and 3.0 and 1.1 for Nd^{3+} and Cs^+ sites, respectively. The surprisingly short Ti/Nb(2)−O(5) bond length and over-bonding for Ti(1) sites may reflect distortions at a more local length scale to optimize bonding within the perovskite blocks (as discussed further below).

3.3. Electron Diffraction and Dark-Field Imaging.

3.3.1. $CsLa_2Ti_2NbO_{10}$. The fundamental reflections in the selected-area electron diffraction (SAED) patterns (Figure 5) for this material can all be indexed by the *a* × *c* unit cell suggested by NPD. However, SAED reveals additional superlattice reflections at the 1/2 *hkl* (*h*,*k*,*l* = odd) position, suggesting ordering (presumably displacive) in the *a*-*b* plane. These reflections exhibited diffuse streaking along the *c*-axis, and the corresponding dark-field images confirmed that the streaks originate from planar defects on the *c*-planes. In some regions, the superlattice spots appeared sharp with the dark-field images highlighting large antiphase domains, while in others, they were very diffuse, indicating that the ordering in such regions is limited to the nanoscale. These observations are consistent with the diffuse-scattering features encountered in the NPD patterns.

3.3.2. $CsNd_2Ti_2NbO_{10}$. The SAED patterns (Figure 6) appear to be inconsistent with the (long-range) $\sqrt{2}a_t \times \sqrt{2}a_t \times 2c_t$ *Pbnm* structure inferred from NPD. For example, sharp spots at 1/2 310 (in *Pbnm* indexes) cannot be accounted

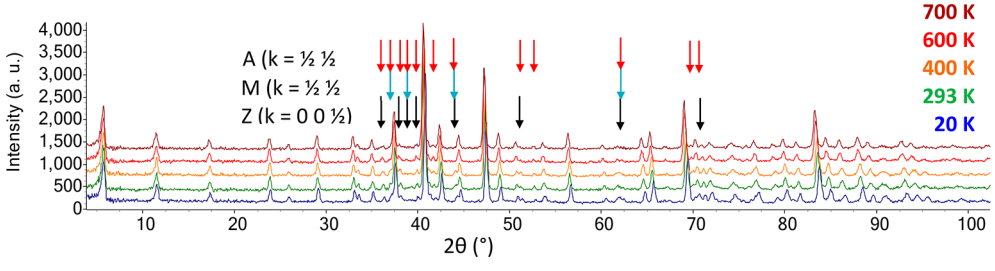

Figure 3. NPD data collected for $CsLa_2Ti_2NbO_{10}$ at 20 (blue, bottom), 293 (green), 400 (orange), 600 (red), and 700 K (brown), showing positions of extra reflections indexed by A, M, and Z-point distortions highlighted by arrows.

https://dx.doi.org/10.1021/acs.chemmater.0c03326
Chem. Mater. 2020, 32, 8700−8712

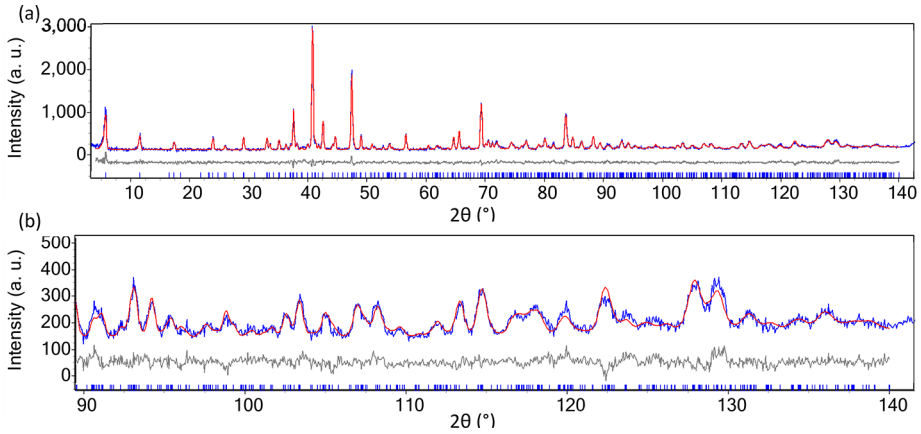

Figure 4. Rietveld refinement profiles for $CsNd_2Ti_2NbO_{10}$ 293 K NPD data fitted with the *Pbnm* model. Observed, calculated, and difference profiles are shown in black, red, and gray with tick marks for the main phase shown in blue. Upper panel (a) shows a whole 2θ range, while the lower panel (b) shows an enlarged high 2θ region.

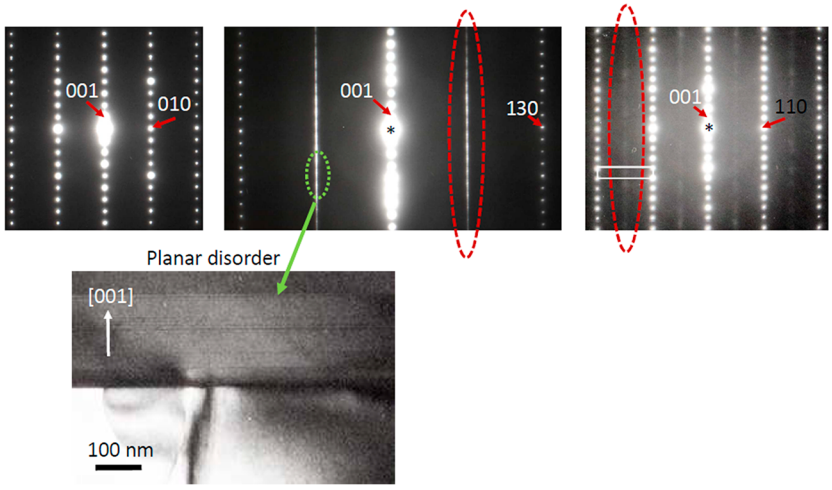

Figure 5. SAED patterns and dark-field imaging for $CsLa_2Ti_2NbO_{10}$ indexed according to the $a_t \times c_t$ ($P4/mmm$) unit cell. Superlattice reflections (e.g., highlighted within red ellipses) indicate displacive ordering in the *a*-*b* plane and dark-field imaging indicates different length scales of this displacive ordering.

for by the $\sqrt{2}a_t \times \sqrt{2}a_t \times 2c_t$ unit cell. At the same time, the *h*0*l* or 0*kl* spots with *l* odd (which are allowed by *Pbnm* symmetry and typically serve as a signature of the coexisting in-phase and out-of-phase rotations) are missing. In fact, all the sharp spots can be indexed by a $2a_t \times 2a_t \times 2c_t$ unit cell. The convergent-beam diffraction and parallel-beam microdiffraction patterns (Figure 7) recorded with the electron beam parallel to the *c*-axis also support the orthorhombic $2a_t \times 2a_t \times 2c_t$ unit cell with the (001) diffraction group 2*mm*. Dark-field images recorded with the 212-type spots highlight antiphase boundaries separating domains a few hundred nanometers in size. In addition to the sharp spots, the SAED patterns contain sets of diffuse reflections near 100-type locations which appear as doublets split along the *c*-axis. Dark-field imaging using these doublets reveals a high number density of planar defects on the *c*-planes. Conceivably, these defects represent antiphase boundaries and/or twins associated with rotations of octahedra along the *c*-axis which form a sequence with a periodicity that is incommensurate with the fundamental lattice parameter thus giving rise to the doublets of spots in SAED. A consistent set of reflection conditions for the sharp spots can only be defined by assuming that the extra spots in the (001) patterns originate from the intersections of the diffuse rods associated with the incommensurate reflections with the (001) reciprocal lattice section. In this case, the reflection conditions are *h*0*l*: *h*,*l* = 2*n*; *hkl*: *h* + *l* = 2*n*; *hk*0: *h*,*k* = 2*n*, which would correspond to a *B*-centered cell. However, possible combinations of low-energy tilts identified from DFT calculations (see below) were considered but did not give models consistent with these reflection conditions. This may indicate combinations of more complex tilts occurring at shorter length scales.

3.4. First-Principles Calculations. Following a similar procedure to that used to study $CsBi_2Ti_2NbO_{10}$,[20] we explored the energy landscape of $CsLa_2Ti_2NbO_{10}$ and $CsNd_2Ti_2NbO_{10}$ by condensing the main unstable phonons and their combinations. To identify instabilities in these systems, we computed the phonon dispersion curves of the high symmetry *P*4/*mmm* phase (Figure 8). Comparison with our previous study on $CsBi_2Ti_2NbO_{10}$[20] reveals similar dispersions for these La and Nd analogues, although fewer unstable modes are present. In addition, the polar branch ($\Gamma_5^- \rightarrow Z_5^-$) is much less unstable for $CsLn_2Ti_2NbO_{10}$ (*Ln* = La, Nd) than for the Bi analogue. This confirms that the nonspherical Bi^{3+} ion is a driving force to enhance ferroelectricity in the Dion-Jacobson systems.

https://dx.doi.org/10.1021/acs.chemmater.0c03326
Chem. Mater. 2020, 32, 8700−8712

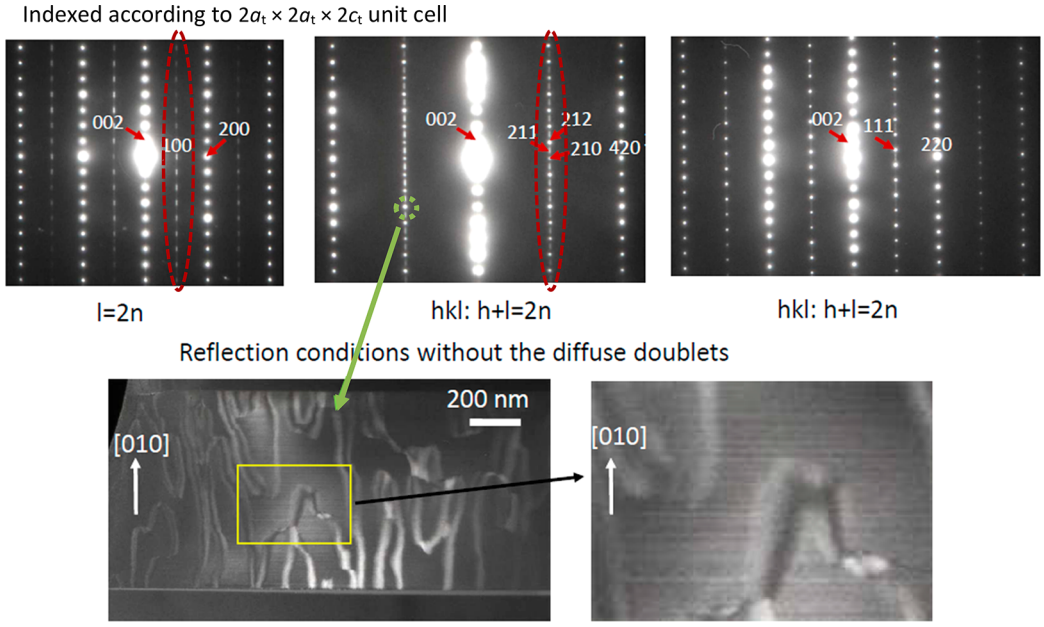

Figure 6. SAED patterns collected at room temperature for $CsNd_2Ti_2NbO_{10}$; superstructure reflections requiring a $2a_t \times 2a_t \times 2c_t$ are highlighted by red ellipses.

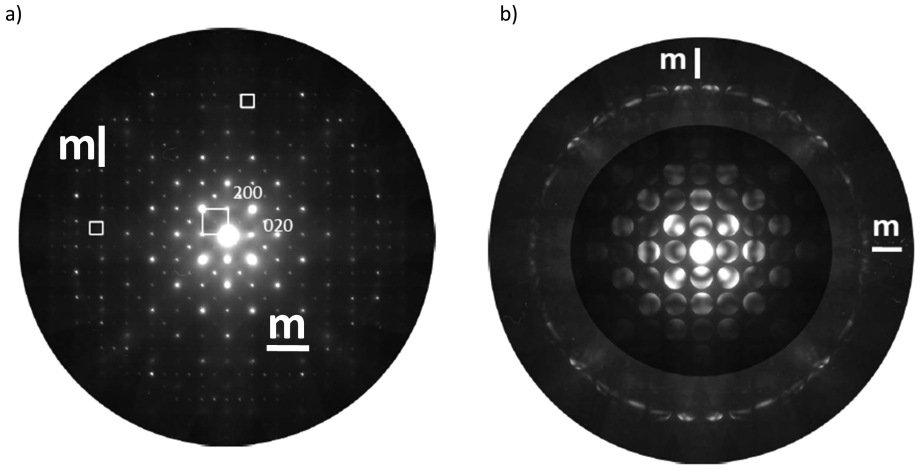

Figure 7. (a) Electron microdiffraction and (b) convergent beam electron diffraction along $[001]_t$ for $CsNd_2Ti_2NbO_{10}$, confirming an orthorhombic and not tetragonal structure and a $2a_t \times 2a_t \times 2c_t$ unit cell with reflection condition $h + k = 2n$.

However, the unstable modes of the *P*4/*mmm* phase cannot indicate which distortions will be dominant. To determine this, we performed single and coupled mode condensations to find which distortions gave the biggest energy gains. The results are reported in the Supporting Information and illustrated in Figure 9.

In general, the gains of energy for Nd and La analogues are noticeably smaller than those for $CsBi_2Ti_2NbO_{10}$ for all distortions (octahedra rotations or in-plane polar/antipolar displacements), giving a much more shallow energy landscape for these two lanthanide analogues.

Considering first in-plane displacements (Γ_5^- and Z_5^-), it is striking that condensing these modes individually gives almost no energy gain in the case of $CsLa_2Ti_2NbO_{10}$ (<3 meV/f.u.) and only a few tens of meV/f.u. in the case of $CsNd_2Ti_2NbO_{10}$, while it is close to 800 meV/f.u. for $CsBi_2Ti_2NbO_{10}$. This difference with Bi can be explained by the fact that polar structures are often favored by the presence of inert-pair Bi^{3+} ions, illustrated by $BiFeO_3$[51] and $Bi_4Ti_3O_{12}$,[19,52] for example. The difference between La and Nd analogues (Nd favoring ferroelectricity more strongly than La) can be ascribed to steric (or geometric) ferroelectricity as reported in strongly ionic perovskites[53] where small cation sizes enhance ferroelectricity (in contrast to conventional charge transfer ferroelectricity as in $BaTiO_3$).[53] This is confirmed by the computer experiment for the smaller *Ln* cation analogue where the energy gains of Γ_5^- and Z_5^- distortions are stronger than for Nd (but still smaller than for Bi, see data table in the Supporting Information), similar to results of calculations on the $n = 2$ DJ phases.[16] In all these cases, the polarization is strongly dominated by *Ln*-O motions and not by the central *B*-cation of perovskite-like blocks, consistent with the optimization of the *A* cation coordination environment (in terms of sterics or electronic factors) driving these cation-displacement distortions.

The octahedral rotations (A_5^+, M_5^+, A_3^+, M_3^+, A_1^-, A_2^+; see the Supporting Information for illustrations) are the dominant distortions governing the crystal phases for *Ln* = La and Nd.

https://dx.doi.org/10.1021/acs.chemmater.0c03326
Chem. Mater. 2020, 32, 8700−8712

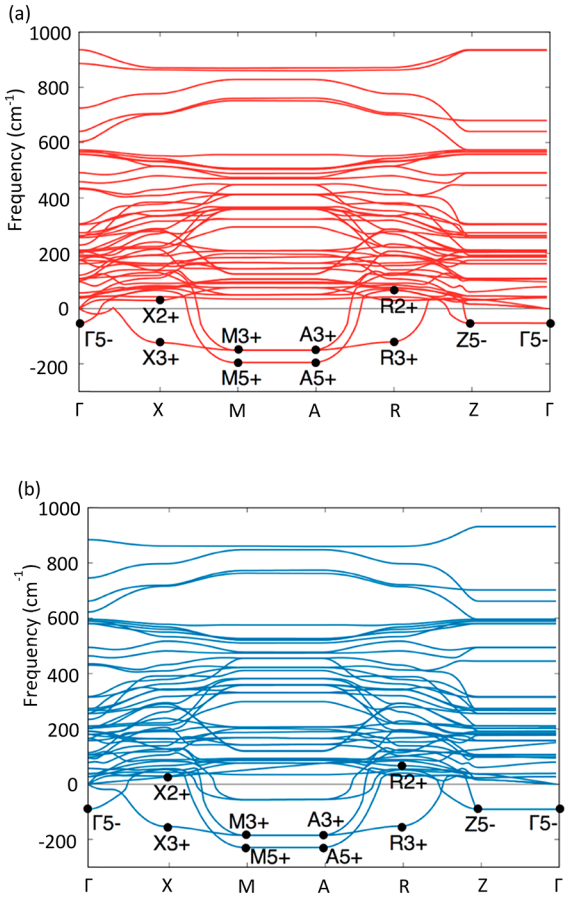

Figure 8. Calculated phonon dispersion curves of $CsLa_2Ti_2NbO_{10}$ (a) and $CsNdTi_2NbO_{10}$ (b) in their high-symmetry phase with space group *P*4/*mmm*. Negative frequencies correspond to imaginary eigenvalues of the dynamical matrix (unstable modes). The label of the unstable modes at zone center and zone boundary points (Γ_5^-, X_3^+, M_5^+, M_3^+, A_5^+, A_3^+, R_3^+, and Z_5^-) is represented on the plots close to their position. The lowest frequency X_2^+ and R_2^+ mode label positions are also shown.

The other *Ln* cases indicate that, as for bulk perovskites, smaller *A*-cations enhance the octahedral rotations such that the energy gain for these rotations increases with decreasing *A* cation size (i.e., it increases for La → Lu, see Figure 10 for the A_5^+ and A_3^+ modes) in the n = 3 DJ systems. The octahedra rotations are the dominant distortions in these n = 3 lanthanide systems, but when in-plane and out-of-plane rotations are present (such as A_5^+ with A_1^-, or M_5^+ with M_1^- for example), (hybrid)-improper ferroelectricity may be allowed by symmetry. However, this is in contrast with the Bi case where polar displacements (ferroelectricity) drive larger energy gains than octahedral rotations such that $CsBi_2Ti_2NbO_{10}$ is much closer to a proper ferroelectric, while any polar nature of *Ln* = La and Nd analogues is mostly driven by an improper origin. (All the lowest energy phases found for La and Nd analogues from DFT calculations are predicted to be improper ferroelectrics.) We also note that the X_3^+ and R_3^+ modes (more complex rotations about an in-plane axis) give less energy gain than similar modes at M and A points. Likewise, the X_2^+ and R_2^+ modes (modes involving rotations of only outer octahedra about the out-of-plane axis) are low frequency modes in the DFT calculations but are not unstable. In all cases (*Ln* = *Pm*−Yb) but specifically for *Ln* = La, Pr, and Nd, rotations about an in-plane axis (A_5^+ and M_5^+ modes) give stronger energy gains than rotations about the out-of-plane axis (A_3^+ and M_3^+). The energy gain from A_5^+ rotations increases more dramatically than that for A_3^+ rotations with decreasing *Ln* size (Figure 10), so that A_3^+ dominates for larger La and Nd, while A_5^+ dominates for smaller ions. These rotations of octahedra occur to optimize cation coordination environments (particularly for the *A* cation in the perovskite layers) and to relieve strain in stacking the perovskite and *A*′ layers of different widths. A_5^+ modes might relieve stacking strain to a greater extent than A_3^+ modes and so become more significant as *A* cations decrease in size, in the presence of the large Cs^+ ion on *A*′ sites. The low-energy phase of *Pnma* symmetry predicted by DFT calculations for $CsNd_2Ti_2NbO_{10}$ (Figure 9) is consistent with the long-range, average structure proposed above from 20−600 K NDP data for $CsNd_2Ti_2NbO_{10}$. It would be interesting to see the effect of

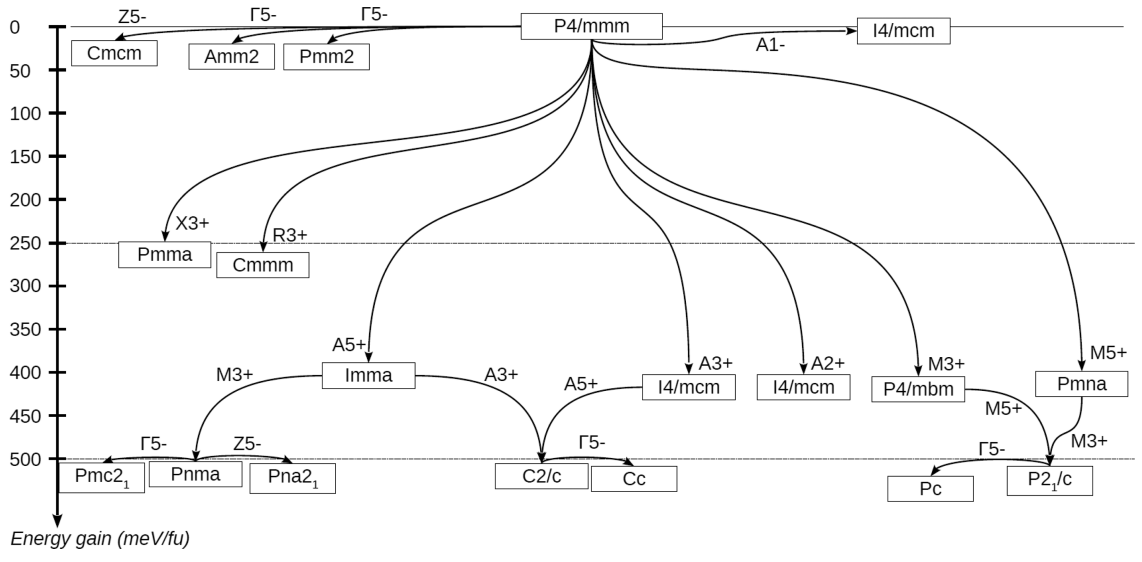

Figure 9. Schematic showing energy gains from different distortion modes and combinations of modes for $CsNd_2Ti_2NbO_{10}$ from DFT calculations.

https://dx.doi.org/10.1021/acs.chemmater.0c03326
Chem. Mater. 2020, 32, 8700−8712

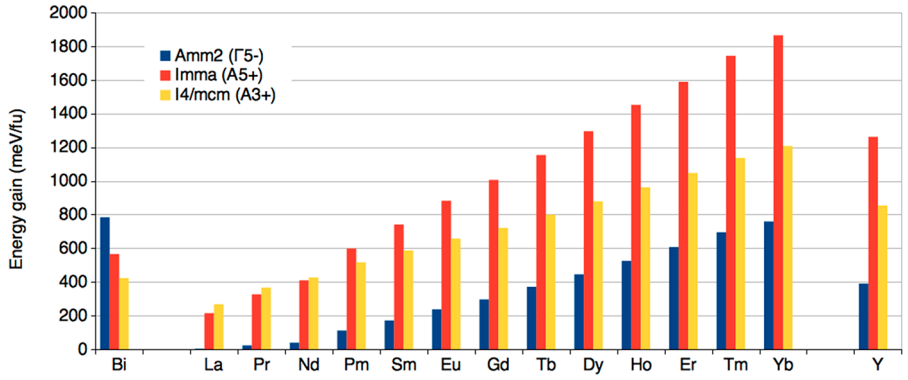

Figure 10. Schematic showing calculated energy gains for A_5^+ ($a^-a^-c^0$) and A_3^+ ($a^0a^0c^-$) rotation modes and Γ_5^- (in-plane polar displacements) for $CsLn_2Ti_2NbO_{10}$ for different *Ln* analogues from DFT calculations.

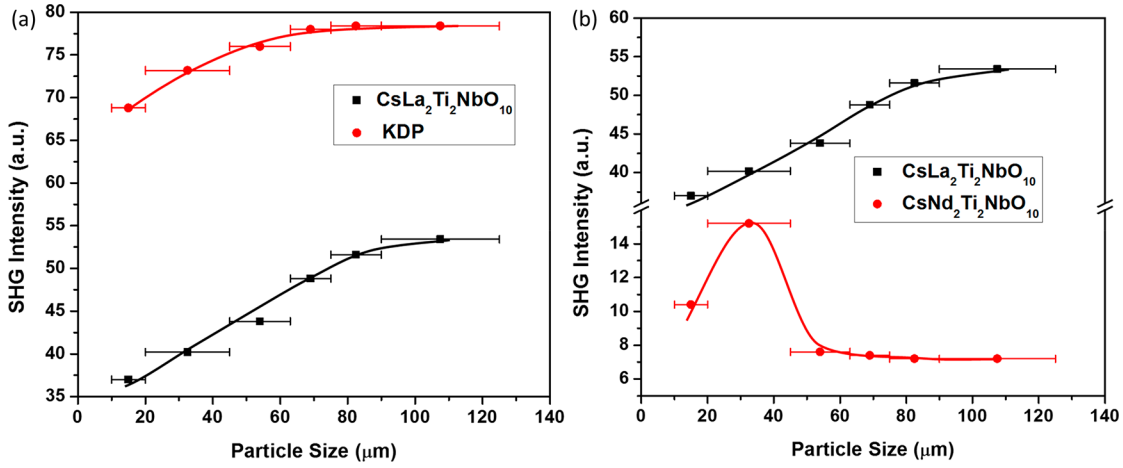

Figure 11. SHG signal as a function of particle size for (a) $CsLa_2Ti_2NbO_{10}$ and compared with KDP and (b) for $CsLa_2Ti_2NbO_{10}$ and $CsNd_2Ti_2NbO_{10}$.

smaller Rb^+ ions of the *A*′ on the relative energies of the A_3^+ and A_5^+ modes.

Consideration of the phonon dispersion for these $n = 3$ DJ phases indicates that there is a lack of dispersion between *M* (1/2 1/2 0) and *A* (1/2 1/2 1/2) points and between Γ (0 0 0) and Z (0 0 1/2). This highlights the limited structural connectivity along $[001]_t$ between successive perovskite-like blocks. As a consequence, often very similar energy gains are observed for different distortions, i.e., rotation modes that are in-phase from block to block (*M* modes) and those that are out-of-phase from block to block (*A* modes) give similar energy gains. (*M* modes are very slightly more stable for *Ln* = La, Nd, while *A* modes are slightly favored for *Ln* = Y, Bi, but these differences are very subtle.) This suggests that such DJ phases show similar behavior to the $Sr_{n+1}Ti_nO_{3n+1}$ Ruddlesden−Popper phases investigated by Birol et al. in which the rocksalt-like SrO layers break the connectivity between perovskite-like layers, reducing the out-of-plane correlation length of (polar) distortions and giving rise to a large number of degenerate, uncorrelated polar regions.[15]

3.5. Physical Properties. *3.5.1. Dielectric Measurements.* The dielectric response of $CsLa_2Ti_2NbO_{10}$ and $CsNd_2Ti_2NbO_{10}$ was measured (see the Supporting Information) and indicated that both ceramics are leaky (with frequency dispersion of tan δ). The permittivity measured was fairly low but increased with temperature as the ceramics became increasingly conducting. Within the temperature range measured (300−800 K), no maximum in permittivity was observed, and there was close agreement between data collected on warming and on cooling.

3.5.2. Second Harmonic Generation (SHG). Second harmonic generation (SHG) measurements using 1064 nm radiation gave a phase-matcheable signal for $CsLa_2Ti_2NbO_{10}$ (about 0.7 times that of KDP), while the SHG signal for $CsNd_2Ti_2NbO_{10}$ was lower ∼0.2 times that of KDP) and is not phase matcheable (Figure 11). No laser damage was observed for either sample. These results indicate that both materials must adopt acentric structures, at least at the length scale probed by SHG measurements.

3.5.3. Optical Characterization. Diffuse reflectance measurements for $CsLn_2Ti_2NbO_{10}$ (*Ln* = La, Nd) diluted in NaCl show a decrease in reflectance from ∼500 nm, although spectra recorded for $CsNd_2Ti_2NbO_{10}$ are complicated by f-f transitions associated with Nd^{3+} (see spectra in the Supporting Information). The signal for both samples are relatively weak, and its hard to detect a sharp decrease in reflectance. However, after the Kubelka-Monk treatment, the spectra suggest an optical bandgap of ∼2.6(2) eV, similar to optical bandgaps reported for $CsBi_2Ti_2NbO_{10}$ and for $CsBiNb_2O_7$ [3.0(1) eV and ∼3.4 eV, respectively].[20,54]

4. DISCUSSION

The long-range, average structures described above for $CsLn_2Ti_2NbO_{10}$ (*Ln* = La, Nd) share similarities with those

https://dx.doi.org/10.1021/acs.chemmater.0c03326
Chem. Mater. 2020, 32, 8700−8712

reported for $A'Bi_2Ti_2NbO_{10}$ (A' = Cs, Rb),[20,23] with the same B-site cation ordering and similar out-of-center displacements for these ions. For $CsLn_2Ti_2NbO_{10}$, Ti^{4+} preferentially occupies the smaller and higher-symmetry central $B(1)$ site, consistent with its size (six-coordinate ionic radii of 0.605 and 0.64 Å for Ti^{4+} and Nb^{5+}, respectively).[49] In common with many n = 3 layered perovskite-related materials, the B cations in the outer layers of the perovskite blocks in $CsLn_2Ti_2NbO_{10}$ are displaced out-of-center toward the interblock layers, giving shorter B−O apical bond lengths, as reported previously for $CsBi_2Ti_2NbO_{10}$[20] and for n = 3 Aurivillius phases such as $Bi_2Sr_{1.4}La_{0.6}Nb_2MnO_{12}$,[55] $Bi_2Sr_2Nb_{2.5}Fe_{0.5}O_{12}$,[56] and $Bi_4Ti_3O_{12}$.[19] However, the noncentrosymmetric, polar structures reported for $A'Bi_2Ti_2NbO_{10}$ (A' = Cs, Rb)[20,23] differ from the results of NPD analysis described here for $CsLn_2Ti_2NbO_{10}$ (Ln = La, Nd). We will consider first the average structures for $CsLn_2Ti_2NbO_{10}$ (Ln = La, Nd) and distortions that give rise to lower symmetry (polar) regions at shorter length scales, as well as the factors that give rise to the differing origins of polar behavior.

The most striking observation from our DFT calculations for $CsLn_2Ti_2NbO_{10}$ (Ln = La, Nd) is the shallow energy landscape dominated by tilt distortions (Figure 9 and DFT results in the Supporting Information). That tilts are the most significant structural distortions is born out by the average structures determined from NPD analysis (with a disordered oxide sublattice observed for $CsLa_2Ti_2NbO_{10}$ and longer-range correlations for $CsNd_2Ti_2NbO_{10}$). In terms of the shallow energy landscape, Figure 9 illustrates that several tilt modes (including those about in-plane axes and those about $[001]_t$) give similar energy gains, and the structural disorder observed experimentally likely arises from combinations of different tilts occurring in different regions and over different length scales. Our electron diffraction and dark field images show clear evidence of this.

Figure 10 also suggests that with decreasing Ln size, rotations about an in-plane axis (A_5^+ rotations) are increasingly favored, presumably to optimize Ln coordination without significant changes to the interlayer A' cation coordination environment. A simple consideration of the packing of ions within the perovskite blocks can be quantified using the Goldschmidt tolerance factor t.[57] (We note that for the DJ phases, this approach neglects their layered nature and any relaxations that might occur at the edges of the perovskite blocks). Values calculated for $CsLn_2Ti_2NbO_{10}$ (t = 0.974 and 0.942 for Ln = La and Nd, respectively, assuming 3D perovskites of hypothetical composition $Ln[Ti_{0.667}Nd_{0.333}]O_3$] suggest that distortions, such as octahedral rotations, are likely to occur to optimize bonding around the small Ln^{3+} ions.

The significance of octahedral rotations in $CsLn_2Ti_2NbO_{10}$ (Ln = La, Nd) compared with displacive distortions contrasts with $CsBi_2Ti_2NbO_{10}$. For the proper ferroelectric $CsBi_2Ti_2NbO_{10}$, in-plane polar cation displacements form the primary order parameter for the paraelectric−ferroelectric phase transition at ∼820 K, giving the largest energy gains and are clear in the long-range average structure. For $CsLn_2Ti_2NbO_{10}$ (Ln = La, Nd), octahedral rotations give the larger energy gains and are likely to drive any phase transitions and so are key to understanding physical properties.[58]

The lack of dispersion along $[001]_t$ in the DJ phases (see Figure 8 and similar results for $CsBi_2Ti_2NbO_{10}$[20]) is more significant than in other layered perovskite-related systems (e.g., Ruddlesden−Popper[12,15] and Aurivillius families), presumably due to the relatively weakly bound A' ions between the perovskite-like blocks (giving the intercalation chemistry these phases are well-known for). This disrupts the correlation in octahedral rotations between blocks; with the similar energies of possible tilts, this gives increased structural disorder. For example, the disordered structure described above for $CsLa_2Ti_2NbO_{10}$ and broad superstructure reflections (incompatible with the c glide present in models with A_3^+, A_2^+, and A_1^- tilts) at 700 K data for $CsNd_2Ti_2NbO_{10}$ are consistent with disorder and shorter-range translational symmetry along $[001]_t$ within the oxide sublattice.

The average centrosymmetric structures determined from NPD analysis are inconsistent with the observed SHG activity for both samples. However, the lower symmetry structures suggested at shorter length scales by SAED (Figures 5−7), resulting from competition between similar energy tilts, could well include local noncentrosymmetric regions that are SHG active. The shallow energy landscape dominated by octahedral tilts that is revealed by our DFT calculations suggests the presence of short-range noncentrosymmetric regions (giving SHG activity) of a hybrid-improper nature (i.e., resulting from different combinations of octahedral rotations as the primary order parameter). We note that there have been reports of localized regions with polarization and octahedral tilts not observed on NPD length scales in Aurivillius phases,[59−61] suggesting that disorder of the anion sublattice may be a factor in other families of layered perovskite-related materials.

Relaxor ferroelectrics, with frequency dispersion of their permittivity,[62] are usually described in terms of polar nanoregions caused by modulations on the cation sublattice.[63] Experimental and theoretical work on other layered materials has suggested a new class of relaxor ferroelectrics, "digital relaxors".[15,64] In these systems, it is the disorder on the oxide sublattice due to the relatively shallow energy landscape (giving several structures of similar energies due to the 2D nature of these materials with perovskite blocks relatively decoupled) that gives rise to short-range polar regions. The DJ family of materials have potential to display such behavior, and the implications for tuning properties are worth further study. Similarly shallow energy landscapes have been reported for hybrid-improper Ruddlesden−Popper systems and are suggested to influence phase-transition pathways between models with different combinations of tilts.[65]

Contrasting the behavior and structures of $CsLn_2Ti_2NbO_{10}$ (Ln = La, Nd) with $A'Bi_2Ti_2NbO_{10}$ (A' = Cs, Rb)[20,23] indicates that it is possible to tune between proper and hybrid-improper mechanisms in n = 3 Dion-Jacobson phases. The hybrid-improper mechanism in these n = 3 systems relies on more complex tilts that rotate only some octahedra in the perovskite blocks (such as A_1^- or M_1^- modes which rotate only octahedra in the outer layers) and can couple with rotations about an in-plane axis (such as A_5^+ or M_5^+ modes) to break inversion symmetry. Such tilt modes are not physical for n = 2 DJ phases, but a similar balance between mechanisms should still be possible and is hinted at in the relative energies of tilts versus displacements as a function of composition across the series $A'ANb_2O_7$ (A' = Rb, Cs and A = Y, Nd, La, Bi).[16] Recent high-resolution work on the Aurivillius phase $Bi_4Ti_3O_{12}$[19] highlights the importance of these more complex tilt modes and structures.

https://dx.doi.org/10.1021/acs.chemmater.0c03326
Chem. Mater. 2020, 32, 8700−8712

5. CONCLUSIONS

This combined experimental and computational study on the n = 3 DJ phases $CsLn_2Ti_2Nb_{10}$ (Ln = La, Nd) highlights the hybrid-improper character of their polar nature, in contrast to $CsBi_2Ti_2NbO_{10}$.[20] This illustrates the ability to tune between proper and hybrid-improper mechanisms in this family of materials as the relative energies of tilt and displacement distortions are changed by composition. The shallow energy landscape revealed by DFT calculations, with little difference in energy between competing structures, is consistent with the structural disorder revealed by neutron and electron diffraction. These disorder and short-range noncentrosymmetric regions are key to understanding the properties (including second-harmonic generation) and have implications for designing functional materials with properties reliant on competing low energy phases such as relaxors and antiferroelectrics.

■ ASSOCIATED CONTENT

Supporting Information

The Supporting Information is available free of charge at https://pubs.acs.org/doi/10.1021/acs.chemmater.0c03326.

Summary of distortions considered for n = 3 DJ phases, details of variable temperature NPD analysis for $CsLa_2Ti_2NbO_{10}$, Pawley and Rietveld refinements using variable temperature NPD data for $CsNd_2Ti_2NbO_{10}$, relative energies of distorted structures for $CsLn_2Ti_2NbO_{10}$ (Ln = La, Nd, Y, Bi) calculated by DFT, dielectric measurements on $CsLn_2Ti_2NbO_{10}$ (Ln = La, Nd), and optical characterization of $CsLn_2Ti_2NbO_{10}$ (Ln = La, Nd) (PDF)

■ AUTHOR INFORMATION

Corresponding Authors

Eric Bousquet − *Physique Théorique des Matériaux, Q-MAT, CESAM, Université de Liège, B-4000 Sart Tilman, Belgium*; Email: eric.bousquet@uliege.be

Emma E. McCabe − *School of Physical Sciences, University of Kent, Canterbury, Kent CT2 7NH, U. K.*; orcid.org/0000-0001-5868-4570; Email: e.e.mccabe@kent.ac.uk

Authors

Vanessa A. Cascos − *School of Physical Sciences, University of Kent, Canterbury, Kent CT2 7NH, U. K.*

Jennifer Roberts-Watts − *School of Physical Sciences, University of Kent, Canterbury, Kent CT2 7NH, U. K.*

Chloe Skingle − *School of Physical Sciences, University of Kent, Canterbury, Kent CT2 7NH, U. K.*

Igor Levin − *Materials Measurement Science Division, NIST, Gaithersburg, Maryland 20899, United States*; orcid.org/0000-0002-7218-3526

Weiguo Zhang − *Department of Chemistry, University of Houston, Houston, Texas 77204, United States*

P. Shiv Halasyamani − *Department of Chemistry, University of Houston, Houston, Texas 77204, United States*; orcid.org/0000-0003-1787-1040

Martin C. Stennett − *Department of Materials Sciences and Engineering, University of Sheffield, Sheffield S1 3JD, U. K.*; orcid.org/0000-0002-8363-9103

Neil C. Hyatt − *Department of Materials Sciences and Engineering, University of Sheffield, Sheffield S1 3JD, U. K.*

Complete contact information is available at: https://pubs.acs.org/10.1021/acs.chemmater.0c03326

Notes

The authors declare no competing financial interest.

■ ACKNOWLEDGMENTS

We are grateful to the NIST visiting researcher scheme and to the NCNR instrument scientists and support laboratories team for provision of beamtime, expertise, and assistance, and to Dr. P. Zajdel for assistance collecting NPD data. We thank funding agencies including the Royal Society (equipment grant RG130844, international exchange scheme IES\R3\170112), The Leverhulme Trust (RPG-2017-362), and EU Cost Action "Towards oxide-based electronics". P.S.H. and W.Z. thank the Welch Foundation (grant E-1457) for support. Computational resources are provided by the Consortium des Equipements de Calcul Intensif (CECI) funded by the F.R.S-FNRS (Grant 2.5020.11) and the Tier-1 supercomputer of the Fédération Wallonie-Bruxelles funded by the Walloon region (Grant 1117545). This research was supported by the HADES/MIDAS facility at the University of Sheffield established with financial support from EPSRC and BEIS, under Grant EP/T011424/1.[66]

■ REFERENCES

(1) Uchino, K. Glory of piezoelectric perovskites. *Sci. Technol. Adv. Mater.* 2015, *16*, DOI: 10.1088/1468-6996/16/4/046001.

(2) Courjal, N.; Bernal, M.-P.; Caspar, A.; Ulliac, G.; Bassignot, F.; Gauthier-Manuel, L.; Suarez, M., Lithium niobate optical waveguides and microwaveguides. In *Emerging waveguide technology* [Online]; You, K. Y., Ed.; IntechOpen, 2018 https://www.intechopen.com/books/emerging-waveguide-technology/lithium-niobate-optical-waveguides-and-microwaveguides (accessed July 23, 2020).

(3) Scott, J. F. Applications of modern ferroelectrics. *Science* **2007**, *315* (5814), 954−959.

(4) de Araujo, C. A-P.; Cuchiaro, J. D.; McMillan, L. D.; Scott, M. C.; Scott, J. F. Fatigue-free ferroelectric capacitors with platinum electrodes. *Nature* **1995**, *374*, 627−629.

(5) Benedek, N. A.; Rondinelli, J. M.; Djani, H.; Ghosez, P.; Lightfoot, P. Understanding ferroelectricity in layered perovskites: new ideas and insights from theory and experiments. *Dalton Trans.* **2015**, *44*, 10543−10558.

(6) Xu, K.; Lu, X. Z.; Xiang, H. J. Designing new ferroelectrics with a general strategy. *npj Quantum Materials* **2017**, *2*, 1−8.

(7) Cammarata, A.; Rondinelli, J. M. Ferroelectricity from coupled cooperative Jahn-Teller distortions and octahedral rotations in ordered Ruddlesden-Popper manganates. *Phys. Rev. B: Condens. Matter Mater. Phys.* **2015**, *92*, 014102.

(8) Dvorak, V. Improper ferroelectrics. *Ferroelectrics* **1974**, *7*, 1−9.

(9) Bousquet, E.; Dawber, M.; Stucki, N.; Lichtensteiger, C.; Hermet, P.; Gariglio, S.; Triscone, J.-M.; Ghosez, P. Improper ferroelectricity in perovskite oxide artificial superlattices. *Nature* **2008**, *452*, 732−736.

(10) Benedek, N. A.; Fennie, C. J. Hybrid improper ferroelectricity: a mechanism for controllable polarization-magnetization coupling. *Phys. Rev. Lett.* **2011**, *106*, 107204.

(11) Yoshida, S.; Akamatsu, H.; Tsuji, R.; Hernandez, O.; Padmanabhan, H.; Sen Gupta, A.; Gibbs, A. S.; Mibu, K.; Murai, S.; Rondinelli, J. M.; Gopalan, V.; Tanaka, K.; Fujita, K. Hybrid improper ferroelectricity in (Sr,Ca)3Sn2O7 and beyond: universal relationship between ferroelectric transition temperature and tolerance factor in n = 2 Ruddlesden-Popper phases. *J. Am. Chem. Soc.* **2018**, *140*, 15690−15700.

(12) Yoshida, S.; Fujita, K.; Akamatsu, H.; Hernandez, O.; Sen Gupta, A.; Brown, F. G.; Padmanabhan, H.; Gibbs, A. S.; Kuge, T.; Tsuji, R.; Murai, S.; Rondinelli, J. M.; Gopalan, V.; Tanaka, K.

Ferroelectric Sr3Zr2O7: competition between hybrid improper ferroelectric and antiferroelectric mechanisms. *Adv. Funct. Mater.* **2018**, *28*, 1801856.
(13) Ablitt, C.; McCay, H.; Craddock, S.; Cooper, L.; Reynolds, E.; Mostofi, A. A.; Bristowe, N. C.; Murray, C. A.; Senn, M. S. Tolerance factor control of uniaxial negative thermal expansion in a layered perovskite. *Chem. Mater.* **2020**, *32*, 605−610.
(14) Chen, W. T.; Ablitt, C.; Bristowe, N. C.; Mostofi, A. A.; Saito, T.; Shimakawa, Y.; Senn, M. S. Negative thermal expansion in high pressure layered perovskite Ca2GeO4. *Chem. Commun.* **2019**, *55*, 2984−2987.
(15) Birol, T.; Benedek, N. A.; Fennie, C. J. Interface control of emergent ferroic order in Ruddlesden-Popper Srn+1TinO3n+1. *Phys. Rev. Lett.* **2011**, *107*, 257602.
(16) Benedek, N. A. Origin of ferroelectricity in a family of polar oxides: the Dion-Jacobson phases. *Inorg. Chem.* **2014**, *53*, 3769−3777.
(17) Zhu, T.; Cohen, T.; Gibbs, A. S.; Zhang, W.; Halasyamani, P. S.; Hayward, M. A.; Benedek, N. A. Theory and neutrons combine to reveal a family of layered perovskites without inversion symmetry. *Chem. Mater.* **2017**, *29*, 9489−9497.
(18) Zhu, T.; Gibbs, A. S.; Benedek, N. A.; Hayward, M. A. Complex structural phase transitions of the hybrid improper polar Dion-Jacobson oxides RbNdM2O7 and CsNdM2O7 (M = Nb, Ta). *Chem. Mater.* **2020**, *32*, 4340−4346.
(19) Guo, Y.-Y.; Gibbs, A. S.; Perez-Mato, J. M.; Lightfoot, P. Unexpected phase transition sequence in the ferroelectric Bi4Ti3O12. *IUCrJ* **2019**, *6*, 438−446.
(20) McCabe, E. E.; Bousquet, E.; Stockdale, C. P. J.; Deacon, C. A.; Tran, T. T.; Halasyamani, P. S.; Stennett, M. C.; Hyatt, N. C. Proper ferroelectricity in the Dion-Jacobson material CsBi2Ti2NbO10: experiment and theory. *Chem. Mater.* **2015**, *27*, 8298−8309.
(21) Wang, X.; Adhikari, J.; Smith, L. J. An Investigation of Distortions of the Dion-Jacobson Phase RbSr2Nb3O10 and Its Acid-Exchanged Form with 93Nb Solid State NMR and DFT Calculations. *J. Phys. Chem. C* **2009**, *113*, 17548−17559.
(22) Walsh, A.; Payne, D. J.; Egdell, R. G.; Watson, G. W. Stereochemistry of post-transition metal oxides: revision of the classical lone pair model. *Chem. Soc. Rev.* **2011**, *40*, 4455−4463.
(23) Kim, H. G.; Tran, T. T.; Choi, W.; You, T.-S.; Halasyamani, P. S.; Ok, K. M. Two New Non-centrosymmetric n = 3 Layered Dion−Jacobson Perovskites: Polar RbBi2Ti2NbO10 and Nonpolar CsBi2Ti2TaO10. *Chem. Mater.* **2016**, *28*, 2424−2432.
(24) Rietveld, H. M. A profile refinement method for nuclear and magnetic structures. *J. Appl. Crystallogr.* **1969**, *2*, 65−71.
(25) Coelho, A. A. Indexing of powder patterns by iterative use of singular value decomposition. *J. Appl. Crystallogr.* **2003**, *36*, 86−95.
(26) Coelho, A. A. *Topas Academic: General profile and structure analysis software for powder diffraction data*; Bruker AXS: Karlsruhe, Germany, 2012.
(27) Campbell, B. J.; Stokes, H. T.; Tanner, D. E.; Hatch, D. M. ISODISPLACE: a web-based tool for exploring structural distortions. *J. Appl. Crystallogr.* **2006**, *39*, 607−614.
(28) Sears, V. F. Neutron scattering lengths and cross sections. *Neutron news* **1992**, *3*, 26−37.
(29) Ok, K. M.; Chi, E. O.; Halasyamani, P. S. Bulk characterisation methods for non-centrosymmetric materials: second harmonic generation, piezoelectricity, pyroelectricity and ferroelectricity. *Chem. Soc. Rev.* **2006**, *35*, 710−717.
(30) Kortum, D. G.; Braun, W.; Herzog, G. Principles and techniques of diffuse-reflectance spectroscopy. *Angew. Chem., Int. Ed. Engl.* **1963**, *2*, 333−341.
(31) Gonze, X.; Jollet, F.; Abreu Araujo, F.; Adams, D.; Amadon, B.; Applencourt, T.; Audouze, C.; Beuken, J.-M.; Bieder, J.; Bokhanchuk, A.; Bousquet, E.; Bruneval, F.; Caliste, D.; Cote, M.; Dahm, F.; Da Pieve, F.; Delaveau, M.; Di Gennaro, M.; Dorado, B.; Espejo, C.; Geneste, G.; Genovese, L.; Gerossier, A.; Giantomassi, M.; Gillet, Y.; Hamann, D.R.; He, L.; Jomard, G.; Laflamme Janssen, J.; Le Roux, S.; Levitt, A.; Lherbier, A.; Liu, F.; Lukacevic, I.; Martin, A.; Martins, C.; Oliveira, M.J.T.; Ponce, S.; Pouillon, Y.; Rangel, T.; Rignanese, G.-M.; Romero, A.H.; Rousseau, B.; Rubel, O.; Shukri, A.A.; Stankovski, M.; Torrent, M.; Van Setten, M.J.; Van Troeye, B.; Verstraete, M.J.; Waroquiers, D.; Wiktor, J.; Xu, B.; Zhou, A.; Zwanziger, J.W.; et al. Recent developments in the ABINIT software package. *Comput. Phys. Commun.* **2016**, *205*, 106−131.
(32) Gonze, X.; Amadon, B.; Antonius, G.; Arnardi, F.; Baguet, L.; Beuken, J.-M.; Bieder, J.; Bottin, F.; Bouchet, J.; Bousquet, E.; Brouwer, N.; Bruneval, F.; Brunin, G.; Cavignac, T.; Charraud, J.-B.; Chen, W.; Cote, M.; Cottenier, S.; Denier, J.; Geneste, G.; Ghosez, P.; Giantomassi, M.; Gillet, Y.; Gingras, O.; Hamann, D. R.; Hautier, G.; He, X.; Helbig, N.; Holzwarth, N.; Jia, Y.; Jollet, F.; Lafargue-Dit-Hauret, W.; Lejaeghere, K.; Marques, M. A.L.; Martin, A.; Martins, C.; Miranda, H. P.C.; Naccarato, F.; Persson, K.; Petretto, G.; Planes, V.; Pouillon, Y.; Prokhorenko, S.; Ricci, F.; Rignanese, G.-M.; Romero, A. H.; Schmitt, M. M.; Torrent, M.; van Setten, M. J.; Van Troeye, B.; Verstraete, M. J.; Zerah, G.; Zwanziger, J. W. The ABINIT project: impact, environment and recent developments. *Comput. Phys. Commun.* **2020**, *248*, 107042.
(33) van Setten, M.J.; Giantomassi, M.; Bousquet, E.; Verstraete, M.J.; Hamann, D.R.; Gonze, X.; Rignanese, G.-M. The PSEUDO-DOJO: training and grading a 85 element optimized norm-conserving pseudopotential table. *Comput. Phys. Commun.* **2018**, *226*, 39−54.
(34) Hamann, D. R. Optimized norm-conserving Vanderbilt pseudopotentials. *Phys. Rev. B: Condens. Matter Mater. Phys.* **2013**, *88*, No. 085117.
(35) Bellaiche, L.; Vanderbilt, D. Virtual crystal approximation application to dielectric and piezoelectric properties of perovskites. *Phys. Rev. B: Condens. Matter Mater. Phys.* **2000**, *61*, 7877−7882.
(36) Gonze, X.; Lee, C. Dynamical matrices, Born effective charges, dielectric permittivity tensors and interatomic force constants from density functional perturbation theory. *Phys. Rev. B: Condens. Matter Mater. Phys.* **1997**, *55*, 10355−10368.
(37) Wu, X.; Vanderbilt, D.; Hamann, D. R. Systematic treatment of displacements, strains and electric fields in density-functional perturbation theory. *Phys. Rev. B: Condens. Matter Mater. Phys.* **2005**, *72*, No. 035105.
(38) Hamann, D. R.; Rabe, K. M.; Vanderbilt, D. Generalized-gradient-functional treatment of strain in density-functional perturbation theory. *Phys. Rev. B: Condens. Matter Mater. Phys.* **2005**, *72*, No. 033102.
(39) King-Smith, R. D.; Vanderbilt, D. Theory of polarization of crystalline solids. *Phys. Rev. B: Condens. Matter Mater. Phys.* **1993**, *47*, 1651−1654.
(40) Glazer, A. M. The classification of tilted octahedra in perovskites. *Acta Crystallogr., Sect. B: Struct. Crystallogr. Cryst. Chem.* **1972**, *B28*, 3384−3392.
(41) Woodward, P. M. Octahedral tilting in perovskites. 1. Geometrical considerations. *Acta Crystallogr., Sect. B: Struct. Sci.* **1997**, *B53*, 32−43.
(42) Howard, C. J.; Stokes, H. T. Group-theoretical analysis of octahedral tilting in perovskites. *Acta Crystallogr., Sect. B: Struct. Sci.* **1998**, *B54*, 782−789.
(43) Aleksandrov, K. S. A2BX4. *Kristallographia* **1987**, *32*, 937.
(44) Aleksandrov, K. S.; Bartolome, J. Octahedral tilt phases in perovskite-like crystals with slabs containing an even number of octahedral layers. *J. Phys.: Condens. Matter* **1994**, *6*, 8219−8235.
(45) Hatch, D. M.; Stokes, H. T.; Aleksandrov, K. S.; Misyul, S. V. Phase transitions in the perovskite-like A2BO4 structure. *Phys. Rev. B: Condens. Matter Mater. Phys.* **1989**, *39*, 9282.
(46) Aleksandrov, K. S.; Beznosikov, B. V.; Misyul, S. V. Successive phase transitions in crystals of K2MgF4-type structure. *Phys. Status Solidi A* **1987**, *104*, 529−543.
(47) Aleksandrov, K. S. Structural phase transitions in layered perovskite-like crystals. *Kristallographia* **1995**, *40*, 279−301.
(48) Brown, I. D.; Altermatt, D. Bond-valence parameters obtained from a systematic analysis of the inorganic crystal structure database. *Acta Crystallogr., Sect. B: Struct. Sci.* **1985**, *B41*, 244−247.
(49) Shannon, R. D. Revised effective ionic radii and systematic studies of interatomic distances in halides and chalcogenides. *Acta*

https://dx.doi.org/10.1021/acs.chemmater.0c03326
Chem. Mater. 2020, 32, 8700−8712

Crystallogr., Sect. A: Cryst. Phys., Diffr., Theor. Gen. Crystallogr. **1976**, *A32*, 751.
(50) Warren, B. E. X-ray diffraction in random layer lattices. *Phys. Rev.* **1941**, *59* (9), 693−698.
(51) Arnold, D. C. Composition-driven structural phase transitions in rare-earth-doped BiFeO3 ceramics: a review. *IEEE Transactions on Ultrasonics, ferroelectrics and frequency control* **2015**, *62*, 62−82.
(52) Aurivillius, B. Mixed bismuth oxides with layer lattices 2: the structure of Bi4Ti3O12. *Arkiv for Kemi* **1949**, *1*, 463−480.
(53) Garcia-Castro, A. C.; Spaldin, N. A.; Romero, A. H.; Bousquet, E. Geometric ferroelectricity in fluoroperovskites. *Phys. Rev. B: Condens. Matter Mater. Phys.* **2014**, *89*, 104107.
(54) Kim, H. G.; Yoo, J. S.; Ok, K. M. Second harmonic generation (SHG) and photoluminescence properties of noncentrosymmetric layered perovskite solid solutions, CsBi1-xEuxNb2O7. *J. Mater. Chem. C* **2015**, *3*, 5625−5630.
(55) McCabe, E. E.; Greaves, C. Structural and magnetic characterisation of Bi2Sr1.4La0.6Nb2MnO12 and its relationship to Bi2Sr2Nb2MnO12. *J. Mater. Chem.* **2005**, *15*, 177−182.
(56) McCabe, E. E.; Greaves, C. Structural and magnetic characterisation of Aurivillius material Bi2Sr2Nb2.5Fe0.5O12. *J. Solid State Chem.* **2008**, *181*, 3051−3056.
(57) Goldschmidt, V. M. Die gesetze der krystallochemie. *Naturwissenschaften* **1926**, *14*, 477−485.
(58) Benedek, N. A.; Fennie, C. J. Why are there so few perovskite ferroelectrics. *J. Phys. Chem. C* **2013**, *117*, 13339−13349.
(59) Wong-Ng, W.; Huang, Q.; Cook, L. P.; Levin, I.; Kaduk, J. A.; Mighell, A. D.; Suh, J. Crystal chemistry and crystallography of the Aurivillius phase Bi5AgNb4O18. *J. Solid State Chem.* **2004**, *177*, 3359−3367.
(60) Goff, R. J.; Lightfoot, P. Structural phase transitions in the relaxor ferroelectric Pb2Bi4Ti5O18. *J. Solid State Chem.* **2009**, *182*, 2626−2631.
(61) Kumar, S.; Ochoa, D. A.; Garcia, J. E.; Varma, K. B. R. Relaxor ferroelectric behaviour and structural aspects of SrNaBi2Nb3O12. *J. Am. Ceram. Soc.* **2012**, *95*, 1339−1342.
(62) Cross, L. E. Relaxor ferroelectrics. *Ferroelectrics* **1987**, *76*, 241−267.
(63) Levin, I.; Keeble, D. S.; Cibin, G.; Playford, H. Y.; Eremenko, M.; Krayzman, V.; Laws, W. J.; Reaney, I. M. Nanosclae polar heterogeneities and branching Bi displacement directions in K0.5Bi0.5TiO3. *Chem. Mater.* **2019**, *31*, 2450−2458.
(64) Stone, G.; Ophus, C.; Birol, T.; Ciston, J.; Lee, C.-H.; Wang, K.; Fennie, C. J.; Schlom, D. G.; Alem, N.; Gopalan, V. Atomic scale imaging of competing polar states in a Ruddlesden-Popper layered oxide. *Nat. Commun.* **2016**, *7*, 12572.
(65) Pomiro, F.; Ablitt, C.; Bristowe, N. C.; Mostofi, A. A.; Won, C.; Cheong, S.-W.; Senn, M. S. From first to second order phase transitions in hybrid-improper ferroelectrics through entropy stabilisation. *Phys. Rev. B: Condens. Matter Mater. Phys.* **2020**, *102*, 014101.
(66) Hyatt, N. C.; Corkhill, C. L.; Stennett, M. C.; Hand, R. J.; Gardner, L. J.; Thorpe, C. L. The HADES facility for High Activity Decommissioning Engineering and Science: part of the UK National Nuclear User Facility. *IOP Conf. Ser.: Mater. Sci. Eng.* **2020**, *818*, No. 012022.

https://dx.doi.org/10.1021/acs.chemmater.0c03326
Chem. Mater. 2020, 32, 8700−8712